Durability of antireflective SiO$_2$ coatings with closed pore structure

Erik Zäll [a,b], Stefan Karlsson [c,**], Mikael Järn [d,***], Jonas Segervald [b], Petter Lundberg [b,e], Thomas Wågberg [b,*]

[a] Absolicon Solar Collector AB, Fiskaregatan 11, SE-871 33, Härnösand, Sweden
[b] Umeå University, Department of Physics, Nano for Energy Group, Linnaeus väg 24, SE-901 87, Umeå, Sweden
[c] RISE Research Institutes of Sweden, Division of Built Environment, Department of Building and Real Estate, Glass unit, Vejdes plats 3, SE-352 52, Växjö, Sweden
[d] RISE Research Institutes of Sweden, Division of Bioeconomy and Health, Department of Materials and Surface Design, Drottning Kristinas väg 45, SE-114 28, Stockholm, Sweden
[e] Swedish University of Agricultural Sciences, Department of Wildlife, Fish and Environmental Studies, Skogsmarksgränd, SE-907 36, Umeå, Sweden

ARTICLE INFO

ABSTRACT

The use of antireflective coatings to increase the transmittance of the cover glass is a central aspect of achieving high efficiencies for solar collectors and photovoltaics alike. Considering an expected lifetime of 20–30 years for solar energy installations, the durability of the antireflective surfaces is essential. Here, a novel antireflective SiO$_2$ coating with a hexagonally ordered closed pore structure, produced with an aerosol-based sol-gel method is benchmarked against two commercial coatings; produced with acid etching and sol-gel roll coating. The optical and mechanical properties together with contact angle characteristics were evaluated before and after various durability tests, including climate chamber tests, outdoor exposure, and abrasion. Compared to the commercial antireflective coatings with open pore structures, the novel coating performed in parity, or better, in all tests. Based on the results of humidity freeze and industrial climate chamber tests, it appears that the coating with closed pore structure has a better ability to prevent water adsorption. Additionally, the closed pore structure of the coating seems to minimize the accumulation of dirt and deposits. The abrasion and cleanability test further confirm the advantages of a closed pore structure, showcasing the coating's mechanical durability. While the coatings exhibit similar hardness and reduced elastic modulus, the closed pore coating proves to be even harder after undergoing the industrial climate chamber test, but also slightly more brittle, as indicated by the probability of crack initiation. In summary the closed pore structure is well suited for tempered and arid climates, making it a truly competitive alternative to existing antireflective coatings.

1. Introduction

Solar energy has long been a cornerstone of the sustainable energy discussion, dating back to the Brundtland Report [1], continuing through the United Nation's sustainability goals [2,3] and the Glasgow climate pact [4]. As a sustainable, renewable and versatile form of energy [5], solar energy can provide electricity, heating and cooling, where electricity in the form of photovoltaics (PV) has reached the largest market penetration to date [6]. However, with half of the global energy consumption being heating and cooling [7,8], the potential for solar thermal is huge. Especially for industrial process heat [3,7], where sectors such as food and beverages, wood treatment, paper production,

chemicals, plastic treatment etc. [9], have a demand of heat in temperature regimes that can be supplied by solar collectors [10].

Most solar technologies require highly transparent glass to reach competitive efficiencies, even if they utilize slightly different parts of the solar spectrum [11]. Antireflective (AR) coatings are used to minimize the primary cause of transmittance losses, reflection in the air/glass interfaces. On solar glass, AR coatings commonly consist of a single mesoporous silica layer [12,13] produced by physical vapor deposition [14], chemical vapor deposition [15] or sol-gel processes [16]. Sol-gel processing is getting increased attention due to lower cost, comparable properties, and higher versatility with bottom-up methods like dip-, spin-, and spray-coating [16–19]. The main challenges of sol-gel

---

* Corresponding author.
** Corresponding author.
*** Corresponding author.
E-mail addresses: stefan.karlsson@ri.se (S. Karlsson), mikael.jarn@ri.se (M. Järn), thomas.wagberg@umu.se (T. Wågberg).

processing are upscaling, homogeneity, and reproducibility, where the vacuum techniques are more reliable [18].

By applying single layer sol-gel deposited silica AR coatings the transmittance of the glass is typically increased by 4–6% depending on the wavelength interval investigated [20–27], giving up to 8% higher yield from the solar energy system [28–31]. Consequently, efficient AR coatings are almost universally applied on solar glass, and the research focus has therefore shifted more towards durability and soiling mitigation [32]. The shift is well motivated considering that reports indicate insufficient durability for the desired 25 year lifetime [33] and annual losses due to soiling reach up to 50% in some cases [34,35]. Additionally, due to their sensitivity to scattering, losses associated with soiling have been shown to be considerably larger for concentrating techniques, like solar collectors, than for PV [36,37].

Mechanical and chemical durability of the coatings are key aspects to reach the desirable 25 year lifetime and various strategies e.g., precursor reactivity [38], partial crystallization [39], gel morphology [40,41], enhancement of interfacial reactions for improving film adhesion [42, 43], pore structure [20] and post-deposition treatments [43–47] have been utilized to address this. Also, incorporation of TiO_2 in the silica coatings have been reported to increase durability [48–50], with the added benefit of photocatalytic self-cleaning effects [49,51], but at the expense of a lowered transmittance [49,52].

Soiling is typically adressed through self-cleaning properties associated by either highly hydrophobic surfaces, where efficient removal of dirt is facilitated by droplets sliding over the surface [53], or by very hydrophilic surfaces relying on the formation of a water film prohibiting adhesion [54]. Porous silica coatings attain these properties either intrinsically [33,55–60] or through additives or surface functionalization [24,30,48,49,61–67]. Regardless, these coatings reduce dirt accumulation and associated transmittance losses [35] as well as the need for active cleaning [36]. Furthermore, if combined with tracking [68], nighttime flip [69] or dust screens [56], the effect of soiling is significantly reduced.

In a previous paper we have presented a sol-gel based, superhydrophilic AR coating with hexagonally ordered closed pores [27]. The AR thin film was applied using an aerosol-based deposition technique called nFOG™ [70], combining easy upscaling [71] with pros related to simplicity similar to spray coating [72]. In this paper we study the durability of this AR coating with regard to humidity, heat, abrasion and soiling, and benchmark it against two commercial AR coatings with open pores. We aim to evaluate if the closed pore structure increases durability without the added complexity of previously mentioned methods, while providing insights into factors affecting the durability of AR coatings for solar glass.

2. Experimental section

2.1. Materials

The hexagonal ordered closed pore AR coating was deposited on a commercial 4 mm thick low-iron float glass (FG), i.e., a low-iron flat glass [16] manufactured with the float process [12]. In short, the AR coating was prepared by evaporation-induced self-assembly of a surfactant-templated silica sol deposited by nFOG™ [70]. By careful control of the synthesis parameters and post-processing steps in a climate chamber and calcination oven, a coating with ordered hexagonal pores, a smooth closed surface and an optimum thickness of 105 nm was achieved. A more in depth description of the synthesis is given in a previous paper [27]. The aerosol deposited hexagonal AR coating, herein denoted as "AR_{Aero}", was benchmarked against two commercial coatings deposited on the same kind of substrate. The commercial coatings are produced through acid etching [28,31] and roll coating [73], herein denoted "AR_{Etch}" and "AR_{Roll}", respectively. All samples evaluated were of the size 50 × 50 mm.

2.2. Durability tests

2.2.1. Climate chamber test

The resistance of the coatings to humidity and temperature was evaluated using humidity freeze and damp heat tests in accordance with IEC 62108 [74], as well as an industrially employed climate chamber test described by Allsopp et al. [11], herein abbreviated "CLC". In the humidity freeze test, one cycle constitutes 20 h at 85 ± 2°C and 85 ± 5% relative humidity followed by a 4 h period where temperature is lowered to -40°C for at least 30 min and then increased back to 85°C. This 24 h cycle is then repeated 20 times to complete the test, see IEC 62108 for details [74]. In the damp heat and CLC tests, the conditions are kept constant, at 85 ± 2°C and 85 ± 5% relative humidity for 1000 h in the former, and at 50°C and 100% relative humidity for 3 weeks (504 h) in the latter. In the CLC test, normal tap water was used, while demineralized water with a maximum conductivity of 5 μS/cm was used in the damp heat and humidity freeze tests. The tests were performed in a Vötsch VCL 4010 climate chamber with the samples positioned horizontally. After the CLC test, the samples were stored at 22 ± 2°C and a relative humidity of 40 ± 20%.

2.2.2. Outdoor exposure

Samples were exposed to outdoor conditions by being placed facing south at an angle of 45° in Härnösand, Sweden (latitude 62.63°, longitude 17.94°). The outdoor exposure lasted for 100 days, from the 19th of March to the June 27, 2021. Härnösand is located at the Baltic Sea in a tempered region (humid continental climate, Dfb, according to the Köppen-Geiger climate classification [75]), this entails temperatures below freezing, snow and ice accumulation, thawing, and strong winds.

2.2.3. Sand contamination, cleanability and abrasion resistance

A washing and abrasion protocol inspired by the D3450-15 standard [76] was developed to mimic contamination and cleaning of the AR glass in arid climates. The protocol constitutes pouring 1 g of sand from the Atacama Desert on each sample, followed by tilting them 90°, making most of the sand slide off, before mounting them in an Elcometer 1720 abrasion and washability tester. A 350 g weight, covered in a wet 150 × 40 mm standard cleaning cloth (soaked in water and squeezed once to remove excess water) was mounted in the washability tester. The weight was then pulled 25 cycles (forward and back) over the samples at a speed of 37 cycles/min and a stroke length of 200 mm. The samples were then removed, rinsed with water, and dried with pressurized air. The procedure was repeated 4 times, for a total of 100 washing/abrasion cycles.

2.2.4. Cleaning scheme

Prior to analysis, all samples were rinsed with isopropanol, ethanol and deionized water (herein denoted "clean"), except for samples exposed to the abrasion test which were only rinsed in water (herein denoted "rinsed"). Samples exposed to tests are called "dirty" prior to being cleaned or rinsed. Additionally, an acid based cleaning scheme was used on the samples exposed to the humidity freeze test to remove formed deposits. This entailed submerging the samples in 0.1 M HCl solution, kept at 35°C and pH 1, for 2 h while stirring, after which they were rinsed with deionized water and blow-dried with pressurized air (herein denoted "HCl"). Furthermore, the samples evaluated with regards to mechanical properties (nanoindentation, crack- and scratch resistance) were wiped with two laboratory tissues, one soaked in ethanol 95% and the other dry.

2.3. Analysis and characterization

2.3.1. Transmittance measurements

The direct transmittance spectrum, $T(\lambda)$, at normal incidence was primarily measured with a PerkinElmer Lambda 1050 spectrophotometer over the interval 300–2500 nm, using a step length and slit width of

5 nm. Using $T(\lambda)$, the solar weighted transmittance, T_{SW}, was calculated using [77]

$$T_{SW} = \frac{\int_{\lambda_1}^{\lambda_2} T(\lambda) I_{AM1.5}(\lambda) d\lambda}{\int_{\lambda_1}^{\lambda_2} I_{AM1.5}(\lambda) d\lambda}, \tag{1}$$

where λ_1 and λ_2 span the wavelength interval and $I_{AM1.5}(\lambda)$ is the ASTM G-173 AM1.5 direct solar spectrum [78]. However, the spectra measured on the samples exposed to the abrasion and CLC test were measured over 300–900 nm using a PerkinElmer Lambda 650 and over 300–1100 nm using a PerkinElmer Lambda 25 UV–Vis spectrophotometer, respectively. Note that all transmittance spectra presented are from samples coated on both sides, and that all transmittance spectra and exact T_{SW} can be found in Fig. S1 and Table S1 in supporting information.

2.3.2. Contact angle measurements

Water contact angles were determined using a Dataphysics OCA40 goniometer. In each measurement, a 3 μL droplet of Type 1 water was dispensed on the surface, and using ellipse fitting, the contact angle was determined after the droplet had stabilized. The results are presented as the mean value and standard deviation from both angles of six individual droplets.

2.3.3. Microscopy and spectroscopy characterization

The morphology of the mesoporous silica coatings was evaluated using scanning electron microscopy (SEM), transmittance electron microscopy (TEM), atomic force microscopy (AFM) and standard optical microscopy. High magnification 2D images of the surface were attained using a Carl Zeiss Merlin FESEM (field emission SEM), employing an acceleration voltage of 15 kV and the in-lens secondary electron detector. To avoid charging, the AR_{Aero} coatings were deposited on a silicon wafer, and the commercial coatings were sputtered with 1 nm of iridium prior to imaging. The pore structure of the coatings was investigated with a Jeol TEM 1230 using 80 kV acceleration voltage. The cross-section of the coatings was exposed by cutting an 80 nm thick lamella with a focused ion beam (Thermo Fisher FEI Scios FIB-SEM), which was then attached to a TEM grid for imaging. To investigate the surface topography following the abrasion test, a Park NX-Hivac AFM was used, imaging at a scan rate of 0.1 Hz in non-contact mode. An Olympus BX51 Optical Microscope was used for low magnification images.

The samples exposed to humidity freeze were also analyzed with energy-dispersive X-ray dispersion (EDX) and X-ray photoelectron spectroscopy (XPS) prior to and after HCl cleaning. The EDX measurements were conducted in an Oxford Instrument X-Max equipment installed in the Merlin FESEM, using an acceleration voltage and current of 15 kV and 300 pA, respectively. For the XPS measurements, a Kratos Axis Ultra DLD electron spectrometer with a 150 W monochromatic A1 K_α source was used, which was calibrated with regards to binding energy in line with the ISO 15472:2010 standard [79].

2.3.4. Nanoindentation

The nanoindentation measurements were performed using an Anton Paar NHT² instrument with a Berkovich diamond tip, with the loads 1, 5, 15, 25, 50 and 75 mN, in a linear loading process with the loading/unloading rate (LR) two times the max load P_{max} per min (LR = 2 × P_{max}) and a 10 s pause at P_{max}. The acquisition rate was 10 Hz, the approach speed 4 μm/min, retract speed 6 μ/min, stiffness threshold 500 μN/μm, spring compliance 0.82 mm/N and a frame compliance 0.20 μm/N. The indenter tip shape was calibrated using a fused silica certified standard sample. For each load, 20 indents were made, except for 1 mN where 40 indents were made. In some cases, one or two outlier datapoints were removed from the analyzed data due to unrealistic scattering. The hardness (H) and reduced elastic modulus (E_r) were determined using the Oliver and Pharr method [80].

For each type of AR coating, two samples were measured, and the results presented in this paper are the pooled results of these two samples. The pooled average, $\bar{x}_p$, was calculated according to

$$\bar{x}_p = \frac{\bar{x}_1 n_1 + \bar{x}_2 n_2}{n_1 + n_2}, \tag{2}$$

where $\bar{x}_i$ is the average and n_i is the amount of data of the individual sample i. The error was calculated by the pooled standard deviation,

$$\sigma_p = \sqrt{\frac{(n_1 - 1)\sigma_1^2 + (n_2 - 1)\sigma_2^2}{(n_1 - 1) + (n_2 - 1)}}, \tag{3}$$

where σ_i is the standard deviation of the individual sample i.

2.3.5. Crack resistance

The crack resistance, or sometimes called the crack initiation resistance, was determined from the probability of crack initiation (*PCI*) by counting the number of radial cracks for 15 Vickers microindentations. The crack resistance method is described in detail by Sundberg et al. [81] which follows the original methodology [82,83]. The *PCI* was fitted using the Weibull sigmoidal function,

$$PCI = 1 - e^{-\left(\frac{x}{x_c}\right)^m}, \tag{4}$$

where x is the load (in N), x_c is the characteristic value and m the Weibull modulus. The fitting error (RMSQ) was calculated by the root mean square deviation of the *PCI*,

$$RMSQ = \sqrt{\frac{\sum_i^N \left(PCI_{real} - PCI_{fit}\right)^2}{N}}, \tag{5}$$

where PCI_{real} is the experimental *PCI*, PCI_{fit} is the fitted *PCI*, N is the number of different loads tested in the series and i is the specific load tested in the series.

The microindentations were performed using a Vickers diamond tip in a Micro-Combi Tester from CSM Instruments. In total 15 indents were made for each load in the load range 0–3 N. The measurements were run with an acquisition rate of 10 Hz, loading/unloading rate of two times the max load per minute, holding time of 15 s, approach speed of 8 μm/min, retract speed of 16.6 μm/min, contact force of 30 mN and contact stiffness threshold of 25 mN/μm. A standard steel reference material was used for calibrating the Vickers indenter tip.

2.3.6. Scratch resistance

The scratch resistance was measured using a Rockwell diamond indenter with a tip radius of 100 μm using a CSM Instruments Micro-Combi Tester. The scratches were made in a linear progressive loading for a length of 5 mm with an acquisition rate of 30 Hz. The start load (also defined as the contact load) was 0.03 N, end load 30 N and the speed 20 mm/min, *i.e.*, a loading rate of 119.88 N/min. The Dz sensor was in large range, with approach and retract speeds of 5 and 10 N/s, respectively.

3. Results

3.1. Characterization of pristine coatings

Despite similar antireflective functions, the surface structure of the pristine coatings differs significantly, as is evident from the SEM images in Fig. 1a–c. The surface of the AR_{Aero} coating is smooth and has closed pores, revealing nothing of the underlying ordered hexagonal pore structure (see details in previous publication [27]). In contrast, AR_{Etch} exhibits open pores of 10–20 nm in diameter on an otherwise smooth surface, while the pore structure of AR_{Roll} is very open, randomly oriented, and larger, with pores up to 50 nm, which are still small enough
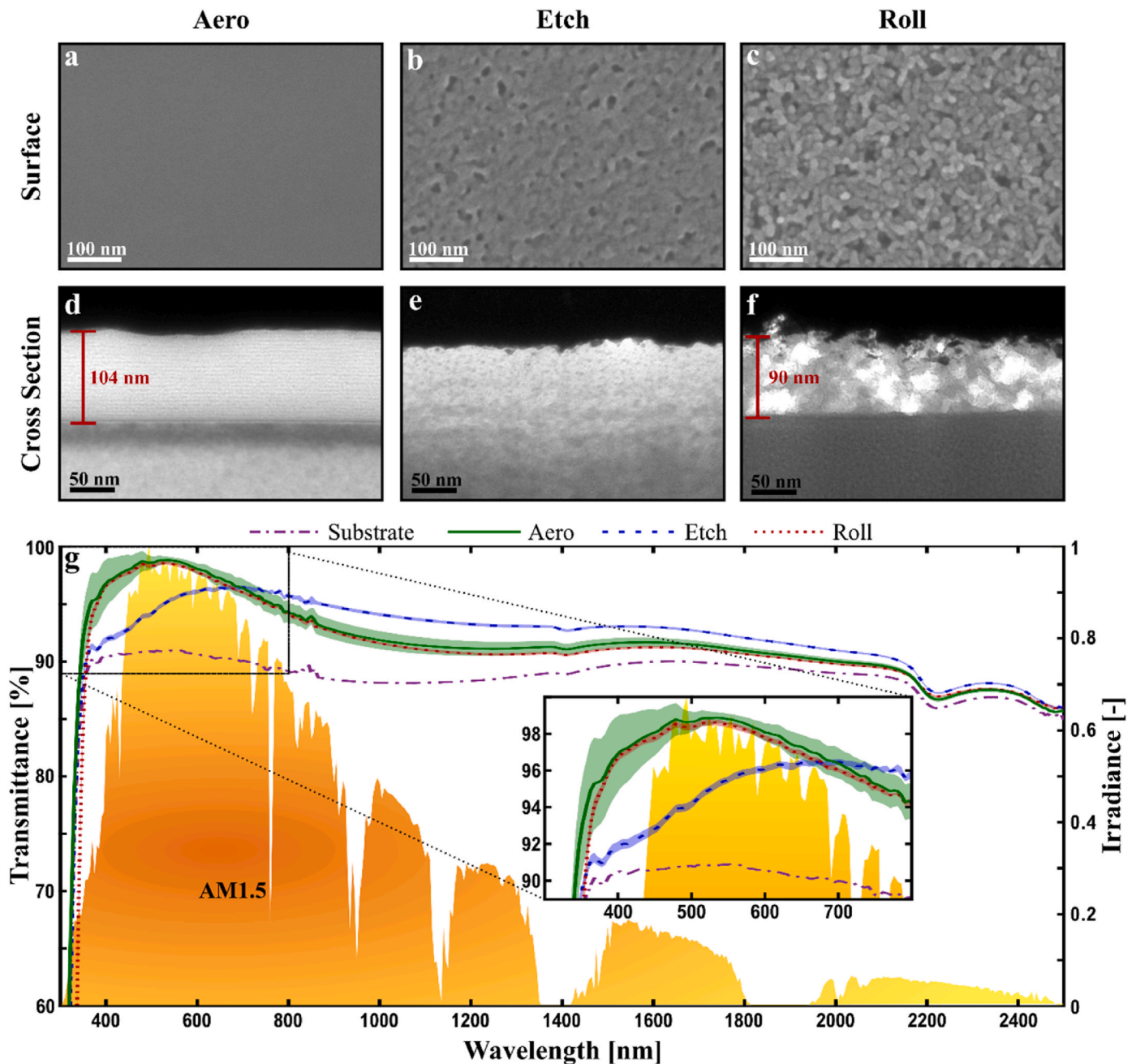
Fig. 1. Morphology and optics of pristine silica coatings. SEM images of the coatings show a smooth surface without open pores for AR_{Aero} (a), open circular pores on an otherwise smooth surface for AR_{Etch} (b) and a randomly oriented open pore structure for AR_{Roll} (c). The cross sections imaged with TEM reveal that AR_{Aero} have elongated horizontally oriented pores and a thickness of ca. 104 nm (d), while AR_{Etch} have a porosity gradient deeper than the thickness of the other coatings (e) and AR_{Roll} is 90 nm thick with larger randomly distributed pores (f). (g) The transmittance spectra of AR_{Aero} and AR_{Roll} are overlapping almost perfectly with a transmittance peak located at 535 nm, well fitted against the intensity of the direct AM1.5 solar spectrum [78], unlike AR_{Etch} for which the transmittance peak is centered around 700 nm and wider due to the thicker gradient porous layer. The shaded areas illustrate one standard deviation for the samples measured (seven for AR_{Aero} and six for AR_{Etch} and AR_{Roll}).

to avoid scattering >300 nm. The open pore structures of AR_{Etch} and AR_{Roll} are typical for AR coatings used on solar glass, where structural design has been overlooked [57]. The differences are attributed to their manufacturing techniques, where AR_{Etch} is produced through acid etching of the glass substrate creating a porous region close to the surface, as opposed to the unordered porosity of the roll coated sol-gel coating of AR_{Roll}.

The cross sections of the AR surfaces manifest the differences further, where the elongated pores parallel to the substrate distinguish AR_{Aero} from the other two, see TEM images in Fig. 1d–f. Both AR_{Aero} and AR_{Roll}

are coatings with a homogenous porosity and a distinct interface to the substrate, while the AR_{Etch} "coating" exhibits a porosity decreasing with depth, a gradient expected for an etched surface [84]. Consequently, defining a coating thickness is not possible for AR_{Etch}, while for AR_{Aero} and AR_{Roll} the thicknesses can be measured to ca. 104 and 90 nm, respectively.

The average transmittance spectra of low iron float glass with and without the AR coatings are presented together with the AM1.5 direct solar spectrum [78] in Fig. 1g. All coatings increase the transmittance significantly, with the most pronounced effect in the visible region,

where transmittance peaks are positioned at 535, 700 and 535 nm for AR_{Aero}, AR_{Etch} and AR_{Roll}, respectively. The difference between AR_{Aero} and AR_{Roll} is marginal outside of peak position, only manifested in a somewhat wider and higher transmittance peak for AR_{Aero}. Using the peak position and thickness (104 nm) of AR_{Aero}, the refractive index of the coating is $n_{Aero} = \lambda/4d = 1.29$, which is in good agreement with reports for hexagonal silica coatings [85] and close to the ideal refractive index of an AR coating, $n_{ideal} = \sqrt{n_{glass}} \approx 1.22$. However, for AR_{Roll} it is $n_{Roll} = 1.49$, which is close to that of soda lime silicate glass [86]. Considering the observed porosity and transmittance, $n_{Roll} \approx 1.2-1.3$ and an average thickness of 100–110 nm is more reasonable, suggesting that the observed 90 nm is an underestimation, see Fig. 1c, f and g. The transmittance peak of AR_{Etch} is significantly wider and shifted to longer wavelengths due to a thicker and gradient porous region, see Fig. 1e.

The solar weighted transmittance (T_{SW}) as calculated by equation (1), of the AR samples are 94.8(3), 94.2(1) and 94.2(2)% for AR_{Aero}, AR_{Etch} and AR_{Roll}, respectively, compared to 89.5% for the low iron float glass substrate. Consequently, the better alignment between solar spectrum and peak position for AR_{Roll} is compensated for by the width of the peak of AR_{Roll}, while AR_{Aero} stands out by having a 5.3% improvement in T_{SW}. This makes AR_{Aero} a competitive AR coating in general [20–26] and even more so among the superhydrophilic ones [33, 58–60].

AR_{Aero} exhibits the lowest contact angle at <5(1)°, compared to 10 (3)° and 8(5)° for AR_{Etch} and AR_{Roll}, respectively, see Fig. 2a and b. Consequently, all three coatings are superhydrophilic [34], which facilitates self-cleaning properties by forming a film of water (see AR_{Aero} in Fig. 2b) mitigating attachment of foulants by transporting them away

with the water [53]. The hydrophilicity is rationalized for high energy silica surfaces [87] by an abundance of hydroxyl groups [88,89]. Other factors affect the wettability as well [35,90], one of which is surface roughness, which as it increases, should decrease the contact angle of an already hydrophilic surface, in accordance with Wenzel's model, suitable for such surfaces [91,92]. However, we observe larger contact angle for rougher surface, which we attribute to contaminants attained from shipping and storage of the commercial samples.

In Fig. 2c and d we see that both the hardness (H) and reduced elastic modulus (E_r) are significantly lower with the AR coatings than for the bare low iron float glass substrate (FG), as is reasonable considering the mesoporous structure. They follow the trend FG > AR_{Etch} > AR_{Roll} > AR_{Aero} for the 1 mN indentation load, reflecting the trend in porosity indicated by Fig. 1, see Table S3 for details. This trend shifts at higher loads, ending up at FG > AR_{Aero} ≥ AR_{Etch} > AR_{Roll} for loads >50 mN, indicating a more homogeneous thickness for AR_{Aero} than the other coatings.

Fig. 2e presents the probability for crack initiation (PCI) as a function of load, demonstrating an improved crack resistance for all AR coatings, as defined by $PCI = 50\%$. The order of crack resistance is AR_{Roll} > AR_{Etch} > AR_{Aero} > FG which reflects both the thickness and porosity of the coatings, see Table S4 for details. As the indenter penetrates the porous AR layer it compresses and densifies, thereby dissipating the mechanical energy of the indenter tip, making the glass beneath less prone to crack. The lower crack resistance of AR_{Aero} can be explained partially by it being thinner and more porous, as indicated by its higher transmittance peak. In general, the AR treated surface acts as a protection against sharp contact damage, as confirmed by the scratch resistance tests in Fig. S2.
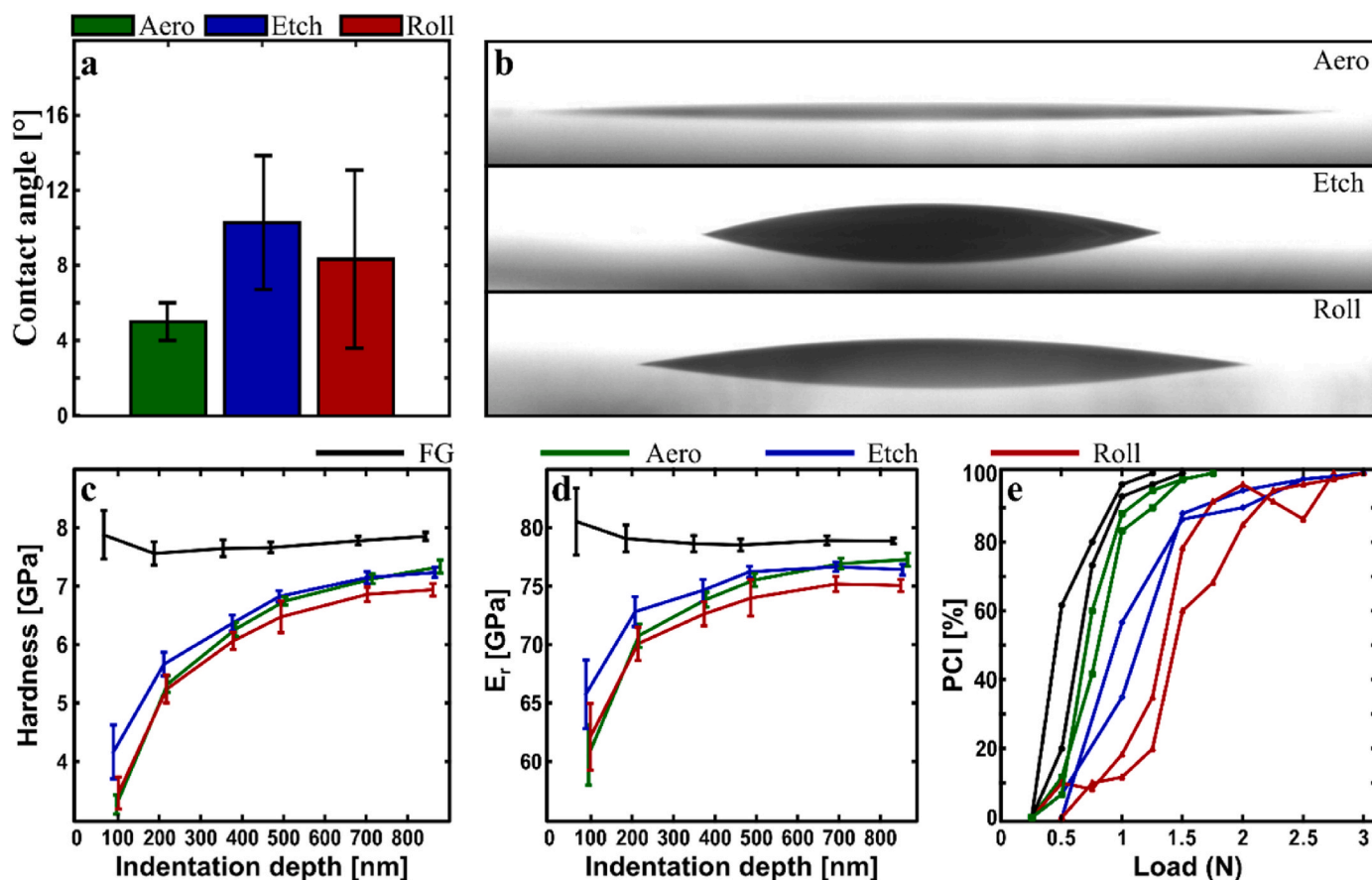

Fig. 2. Water contact angle and mechanical properties of pristine silica coatings. The water contact angle of all three coatings are ≤10° making them superhydrophilic (a), which is also clear from the photos of stable droplets (b). The mesoporous coatings significantly decrease both the hardness (c) and reduced elastic modulus (d) compared to the low iron float glass substrate. The porous AR layers do however decrease the probability for crack initiation as they compress and dissipate the mechanical energy, postponing crack formation (e).

3.2. Humidity freeze

Hydrophilic porous silica surfaces are susceptible to adsorption of water [13,33] and subsequent cracking as it freezes [33], making humidity freeze an important and challenging test [22,34]. Fig. 3 shows SEM images of the surface morphology of the AR coatings following the humidity freeze test (3a-c) and subsequent HCl cleaning (3d-f), see section 2.2.4. AR_{Aero} and AR_{Etch} are less affected than AR_{Roll}. The clean AR_{Etch} sample looks unaffected while minor degradation, exposing pores up to 20 nm in diameter, is visible on the AR_{Aero} sample. The effect of the HCl cleaning is limited to a slight smearing (polishing) of features for both AR_{Etch} and AR_{Aero}. However, AR_{Roll} reveals a largely closed surface with protruding structures, attributed to salt deposits, seemingly penetrating the porous coating for the clean sample. The HCl cleaning removed these features revealing a surface with open pores up to 100 nm in diameter, suggesting that the HCl have polished away the deposits and the top layer of the coating. There are deposits on all samples, but far more on AR_{Roll} than the other two, suggesting a larger susceptibility for the open pore structure. From EDS mapping and XPS we confirm that the deposits are primarily calcium carbonate, $CaCO_3$, see Fig. S3 in supporting information. The $CaCO_3$ originates from evaporation of the water used in the test and is efficiently removed with the HCl cleaning.

In Fig. 3g, we see that the humidity freeze test significantly decreases the T_{SW} for all AR surfaces with largest effect on AR_{Roll}, for which it drops <80% when dirty, before increasing to approximately 82 and 91.5% for the clean and HCl samples, respectively. Both AR_{Aero} and AR_{Etch} exhibit the same trend in T_{SW}, but less pronounced, with transmittance values of 89, 91 and 91.5% for the dirty, clean and HCl
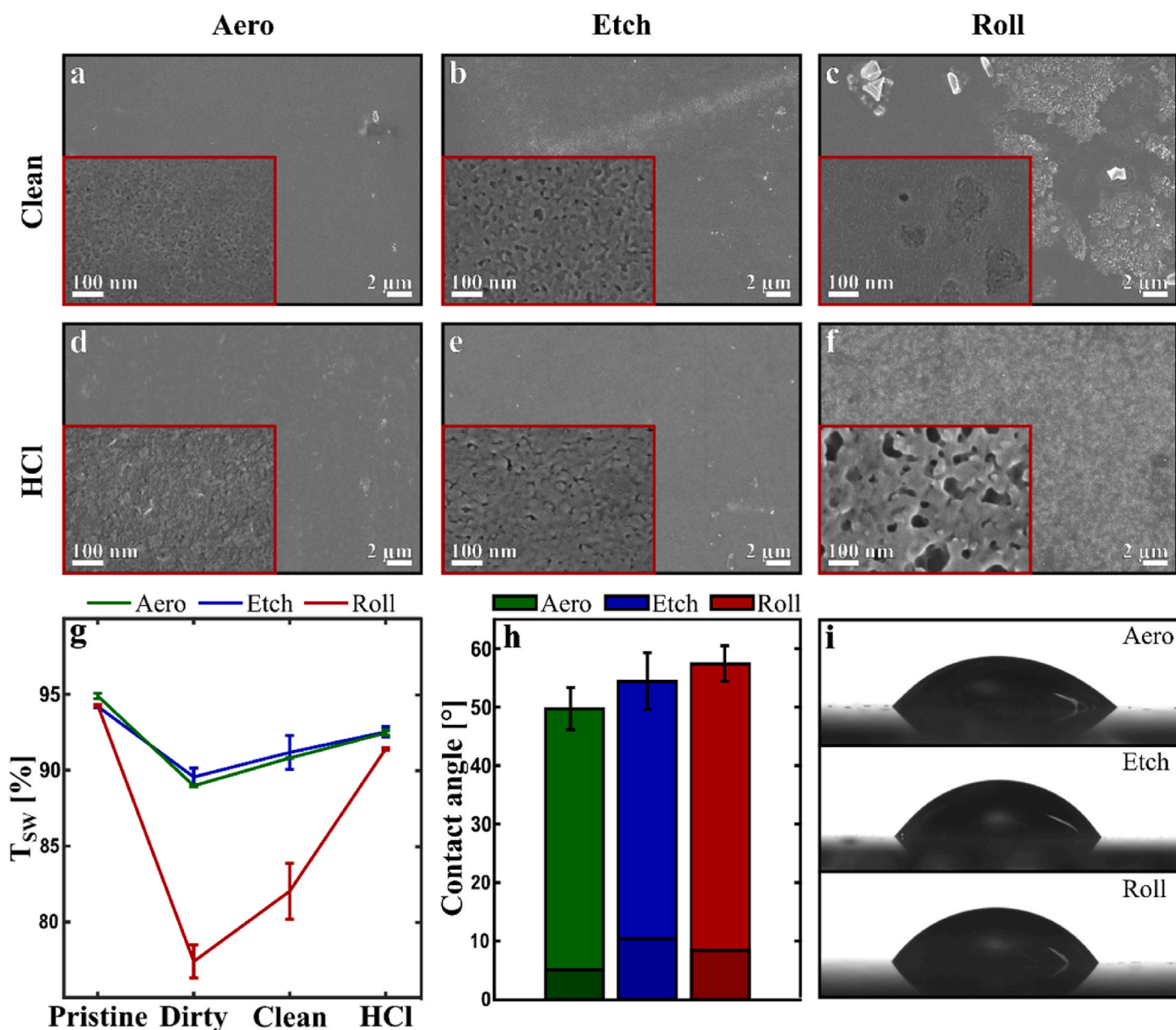

Fig. 3. Characterization after humidity freeze. SEM images of the coating surfaces following the humidity freeze test show that the clean AR_{Aero} and AR_{Etch} samples are largely unaffected (a, b) and that the HCl cleaning has a moderate polishing effect (d, e). However, the surface morphology of AR_{Roll} is affected by the test, as we can see a largely closed surface with significant deposits seemingly penetrating the pore structure of the clean samples (c), while the HCl cleaning have exposed the underlying pores and removed the deposits (f). The average T_{SW} of the coatings drop significantly after the humidity freeze test, before increasing somewhat from the cleaning schemes, with AR_{Roll} performing significantly worse than AR_{Aero} and AR_{Etch} (g). Due to soiling, the water contact angle of all coatings increases significantly from the humidity freeze test, but they are all still hydrophilic (h, i). Note that the darker bars in (h) are the contact angles for the pristine coatings.

samples, respectively.

The limited degradation of AR_{Aero} and AR_{Etch} indicate that, despite being superhydrophilic, significant water penetration, and subsequent damage during freezing, is avoided. For AR_{Aero} the closed pores prohibit water penetration, while we speculate that a low pore interconnectivity in AR_{Etch} limits it sufficiently. This suggests that the open pore structure of AR_{Roll} is more susceptible to water adsorption, which agrees with capillary forces dominating this process under high humidity conditions [13,35].

The difference between the coatings after humidity freeze is less pronounced for the water contact angle, where an increase of roughly 45° is observed for all surfaces, resulting in 50(3)°, 54(5)° and 57(3)° for AR_{Aero}, AR_{Etch} and AR_{Roll}, respectively, see Fig. 3h. Consequently, all are still hydrophilic, which is also apparent from the images of representative stable droplets in Fig. 3i. A limited change in surface morphology, the observed deposit on the samples, and the fact that superhydrophilic silica coatings have been associated with adhesion of foulants [54] due to availability of reactive OH groups [93], suggests that soiling is the primary cause of the increased contact angle.

3.3. Damp heat and industrial climate chamber test

Due to the detrimental effect of water adhesion [13], silica AR coatings are often evaluated after extended exposure to high humidity and temperature in tests like damp heat [20,24,33,48–50,94,95]. In Fig. 4a–c, SEM images reveal significant changes to the surface morphology of the coatings following the damp heat test. The AR_{Aero}

surface exhibits groves up to 200 nm in size, with regions of smaller pores penetrating deeper into the structure. Similar features are visible on AR_{Roll}, but instead of groves the pores are smaller and deeper. The surface of AR_{Etch} instead exhibits a rough, uneven surface with thin ridges and few distinct pores visible, indicating a higher resistance for the etched surface than the deposited coatings. It is apparent that all coatings have degraded, and unlike previous studies [20], the closed pores of AR_{Aero} were insufficient in prohibiting degradation over the extended time of the test. We suggest that our observations correspond to the effect of hydrolysis of the siloxane bond, producing silicic acid, facilitated by agglomeration of water on the surface of the hydrophilic coatings during the test [96–98].

In Fig. 4d we see that the degradation evident in the SEM images is reflected in the average T_{SW} of the coatings, at 90.1(4), 92.2(2) and 91.1 (1)% for the clean AR_{Aero}, AR_{Etch} and AR_{Roll} samples, respectively. In addition to the structural degradation, part of the loss in T_{SW} can be attributed to adsorption of water in the pore structure, which reduces the AR effect by increasing the effective refractive index of the coatings. The larger loss for AR_{Aero} compared to AR_{Roll} can be explained partially by scattering of wavelengths up to approximately twice the maximum size of the groves visible in Fig. 4a, resulting in a significantly lower direct transmittance <700 nm, see Fig. S1c.

Despite its similarities to damp heat, the dip in transmittance for short wavelengths is not present for AR_{Aero} after the industrial climate chamber test, see Fig. S1e. In fact, AR_{Aero} exhibit the highest T_{SW} of the clean coatings after CLC at 91(1)% while AR_{Etch} is still better than AR_{Roll} at 89(1) and 85(5)%, respectively, see Fig. 5a. Consequently, the closed
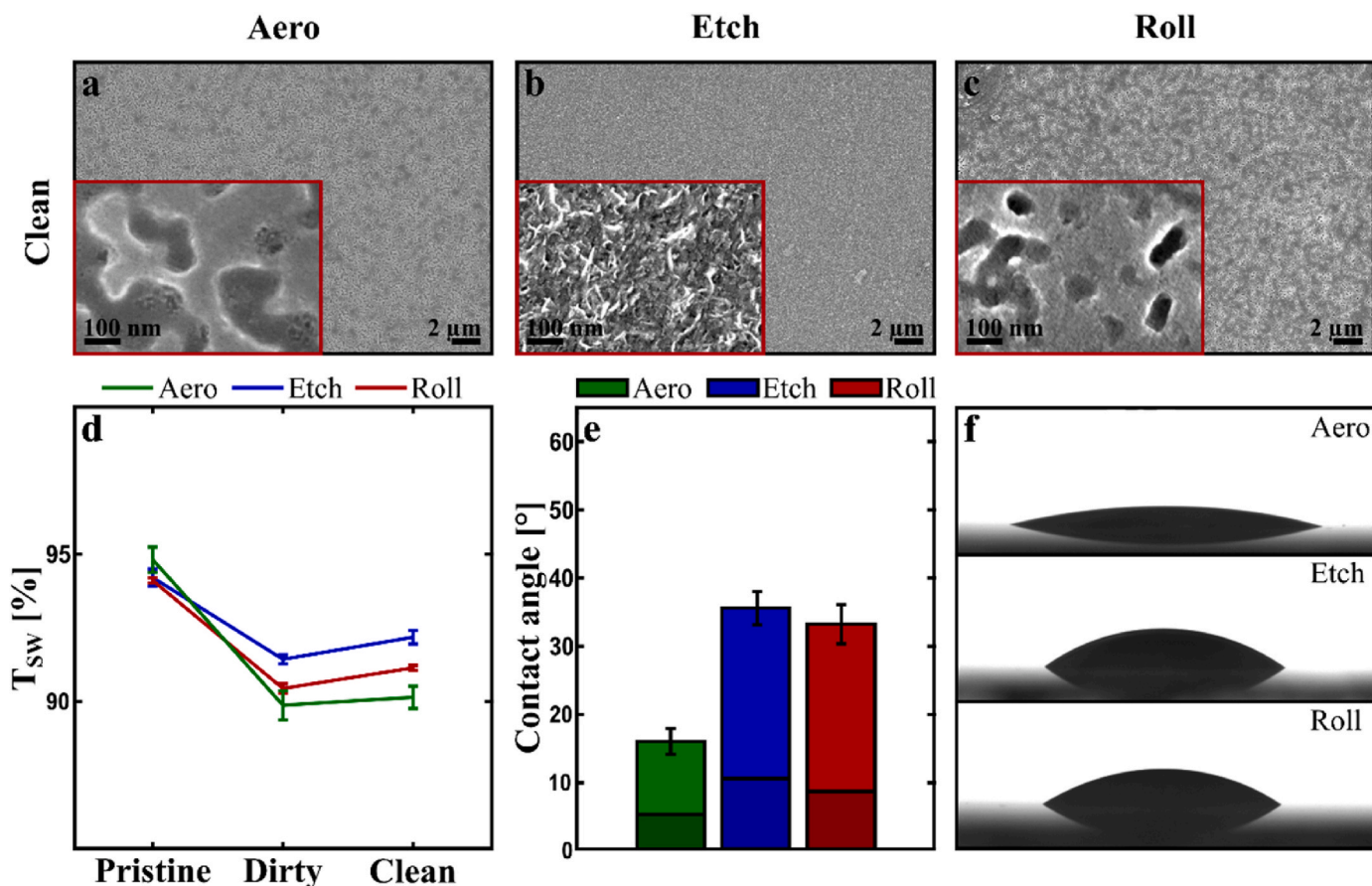

Fig. 4. Characterization after damp heat. The surface morphology of clean coatings is significantly affected by the damp heat test, on AR_{Aero} this is manifested as grooves up to 200 nm in size (a), similarly but smaller pores that penetrate deeper are visible on AR_{Roll} (c), while AR_{Etch} exhibit a rough surface with sharp ridges and only the occasional pore (b). The average T_{SW} of the clean coatings drop to between 90 and 92%, with AR_{Aero} decreasing the most, partially due to scattering of wavelengths <700 nm in the relatively large grooves (d). The water contact angle increases moderately from the pristine case (darker bars) with AR_{Aero} exhibiting a contact angle of 16° while AR_{Etch} and AR_{Roll} are >30° (e), as illustrated by the hydrophilic behavior visible in the photos of stable droplets (f).
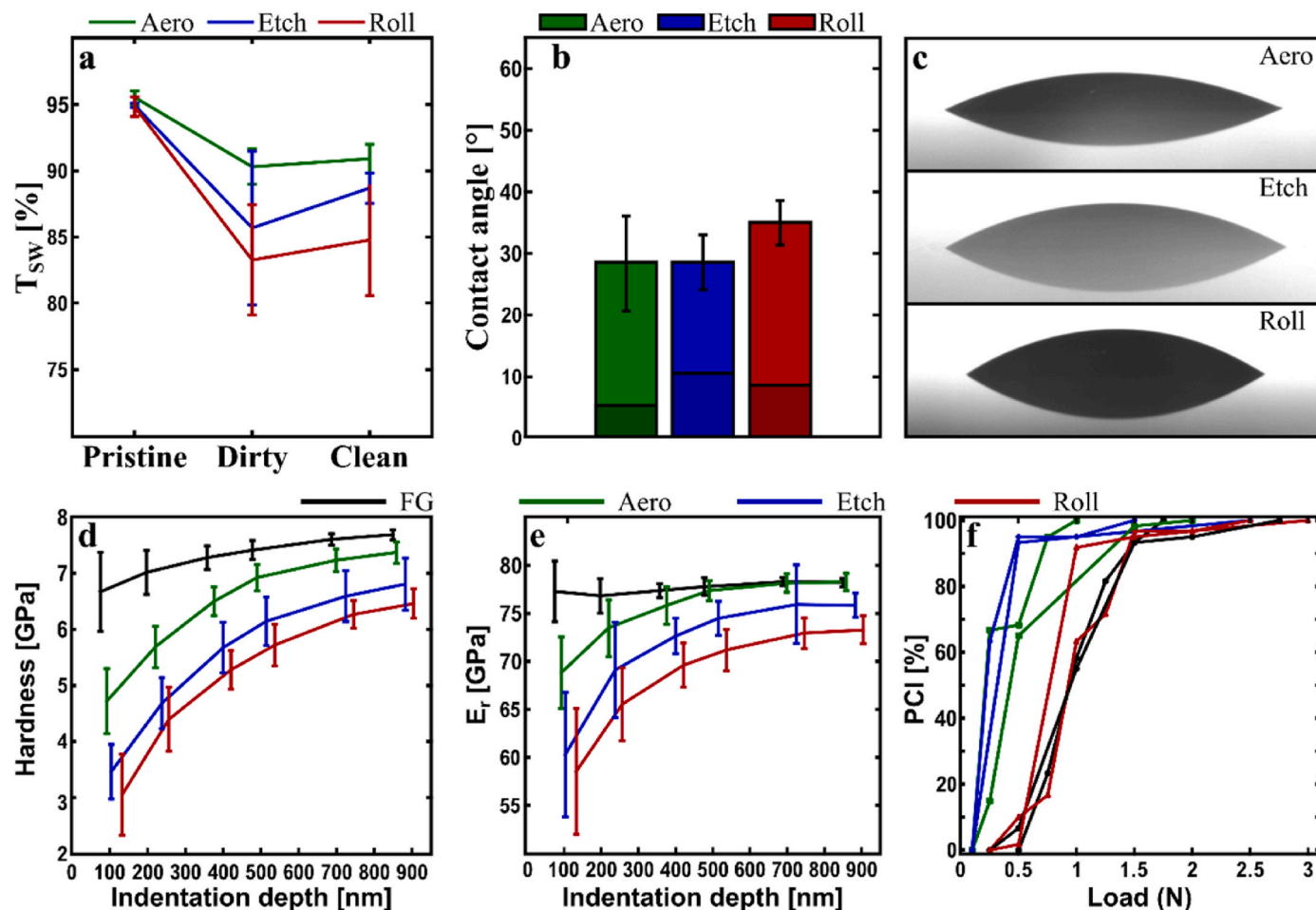
Fig. 5. Characterization after industrial climate chamber test. The average T_{SW} following the CLC test is reduced in accordance with level of open pores, with a small reduction for AR_{Aero}, followed by AR_{Etch} and then AR_{Roll} significantly lower (a). The water contact angle is however similar for all coatings at approximately 30° (b) and still hydrophilic (c). Both hardness (d) and reduced elastic modulus (e) have decreased for FG, AR_{Etch} and AR_{Roll}, as expected, while it has increased for AR_{Aero}. The primary change in the probability for crack initiation compared to the pristine case is that the resistance of the float glass increased due to crack tip blunting (f).

pore structure of AR_{Aero} protects it from hydrolysis more efficiently at the lower temperature and shorter time of the CLC test. The reduction in transmittance is instead largely attributed to soiling from the used tap water, indicating a relation between soiling and an open pore structure.

In Fig. 4e and f we see that all coatings are still hydrophilic after the damp heat test, but AR_{Aero} is significantly less affected with a contact angle of 16(2)° compared to 35(2)° and 33(3)° for AR_{Etch} and AR_{Roll}, respectively. After the CLC test, the results are similar for all coatings at approximately 30°.

In Fig. 5d and e we see that the hardness (H) and elastic modulus (E_r) are significantly affected by the CLC test, with FG, AR_{Etch} and AR_{Roll} exhibiting consistently lower values, rationalized by water penetrating the surface [99]. In contrast, both H and E_r have increased for AR_{Aero}, see specifics in Table S3. Evidently, the closed pore structure of AR_{Aero} prohibits the penetration of water and subsequent softening. In Fig. 5f, the trends of PCI have also changed compared to the pristine case (Fig. 2e), now exhibiting a crack resistance of FG > AR_{Roll} > AR_{Aero} > AR_{Etch}. For FG, the crack resistance is increased due to the humidity causing crack tip blunting [100], while that of the AR coated glasses are lowered, see exact values in Table S4. The AR coatings prevent the softening observed for the substrate by protecting it from the humidity, however, the reason for a lower crack resistance is difficult to deduce without additional characterization, which is outside of the scope of this paper.

3.4. Outdoor exposure

In Fig. 6a–c, the SEM images show that the surface morphology of AR_{Etch} is seemingly unaffected from being subjected to outdoor exposure for 100 days, while AR_{Aero} and AR_{Etch} exhibit minor change compared to the pristine coatings (see Fig. 1a–c). The initially smooth and closed surface of AR_{Aero} now exhibits the occasional open pore in the size of 10–20 nm in diameter, similar but less pronounced than after humidity freeze, while the surface morphology of AR_{Roll} is less granular and more rugged. Even though 100 days is a relatively short time, the climate in Härnösand during the spring constitutes a harsh environment due to temperatures below freezing, snow accumulation, thawing, and strong winds at the coast.

Fig. 6d displays the average T_{SW} of all three coatings decreasing from >94% when pristine to ca. 93% when cleaned after the test, thus exhibiting minor reductions in T_{SW}, in line with literature [55,101]. Considering the largely intact coatings visible in the SEM images, as well as a drop in transmittance distributed over the entire wavelength spectrum (300–2500 nm), see spectra in Fig. S1d, the decreased T_{SW} is attributed to soiling not removed by the applied cleaning scheme. This highlights the need of regular cleaning in the field to avoid accumulation and strong adhesion of dirt, as previously suggested [19].

Following the outdoor exposure, the water contact angle of all coatings increased to approximately 30°, see Fig. 6e. We primarily attribute the observed increase in contact angle to organic
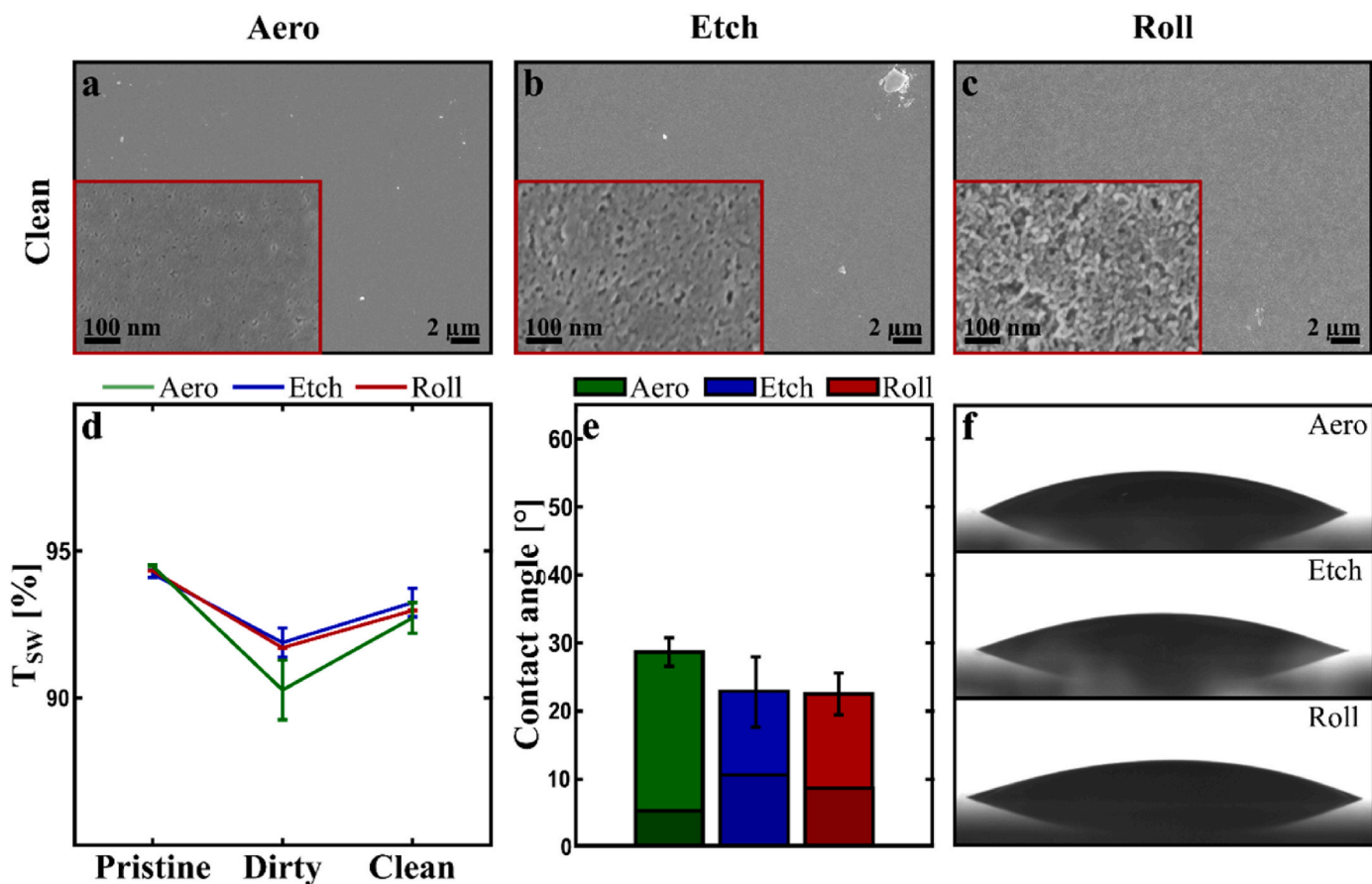
Fig. 6. Characterization after outdoor exposure. As seen in the SEM images, the surface morphology of AR_{Etch} (b) is unaffected by the outdoor exposure, while AR_{Aero} (a) exhibits the occasional small pore not visible on the pristine sample and the surface of AR_{Roll} is somewhat less granular (c). The effect of the outdoor exposure on the average T_{SW} is limited with the clean samples of all coatings at approximately 93% (d). The water contact angle is however similar for all coatings at approximately 30° (e) and still hydrophilic (f).

contamination on the silica surfaces [93]. Regardless, the coatings are all still strongly hydrophilic, retaining the associated benefits of self-cleaning properties and reduced scattering after 100 days outdoors.

3.5. Abrasion resistance and cleanability

Based on the optical microscope images following the abrasion test shown in Fig. 7a–c, AR_{Etch} is less prone to scratching than the deposited sol-gel coatings (AR_{Aero} and AR_{Roll}). The scratching is most severe for AR_{Roll}, which exhibits scratches of several μm in width and regions where the coating has detached. Scratches are also clearly visible on AR_{Aero}, but less pronounced than AR_{Roll}. Unlike AR_{Aero} and AR_{Roll}, AR_{Etch} exhibit numerous point defects and stuck grains of sand, seen as dark spots in the microscope (Fig. 7b), resembling observations of sand blasted solar glass [102]. The lack of visible grains of sand could indicate a better cleanability for AR_{Aero} compared to AR_{Etch}, as expected for the smoother surface [103], while the same is true relative AR_{Roll} due to number of scratches.

The corresponding AFM scans, shown as insets in Fig. 7a–c, further supports that it is distinct scratches associated with grains of sand sliding across the surface, with smooth and seemingly unaffected coating between the scratches. However, from the profile it is apparent that the depth of the scratches varies, being approximately 65, 120 and 110 nm deep for AR_{Aero}, AR_{Etch} and AR_{Roll}, respectively. For AR_{Roll}, the depth agrees with the expected thickness of the coating (though larger than observed in Fig. 1f), which together with the flat bottoms suggest that the coating has been removed down to the substrate, in line with other reports [104]. However, the scratch depth of AR_{Aero} is smaller than the

coating thickness, suggesting that the smooth and closed structure is more resistant to wear than AR_{Roll}.

In terms of optical performance, T_{SW} have changed from 96.6(1), 95.2(1) and 96.1(0)% before the abrasion test to 95.8(2), 94.3(2) and 94.8(1)% after, for AR_{Aero}, AR_{Etch} and AR_{Roll}, respectively, see Fig. 7d. Evidently, the less pronounced point defects of AR_{Etch} have a significant optical effect. Note that the spectra are measured in the interval 300–900 nm, promoting AR_{Aero} and AR_{Roll} over AR_{Etch} in terms of total transmittance, see Fig. S1f.

In Fig. 7e and f we observe that all coatings are still hydrophilic, with contact angles of 25(5), 24(10) and 14(11)° for AR_{Aero}, AR_{Etch} and AR_{Roll}, respectively, making AR_{Roll} the least increased despite the significant mechanical degradation seen in the microscope.

4. Discussion

Overall, the AR_{Aero} coating demonstrates comparable, or even superior performance to the commercial coatings, as can be seen in Fig. 8, with some results indicating benefits associated with the closed pore structure. The humidity freeze and industrial climate chamber tests suggest an ability to prohibit water adsorption and that the closed pore structure reduces soiling from deposits despite the high wettability. The abrasion and cleanability test also support the notion of a closed pore structure being beneficial [103], and highlight the mechanical durability of the coating. The hardness and reduced elastic modulus of the coatings are similar, but after the industrial climate chamber test the AR_{Aero} coating is harder, and based on the probability for crack initiation, slightly more brittle. The only test where AR_{Aero} exhibited
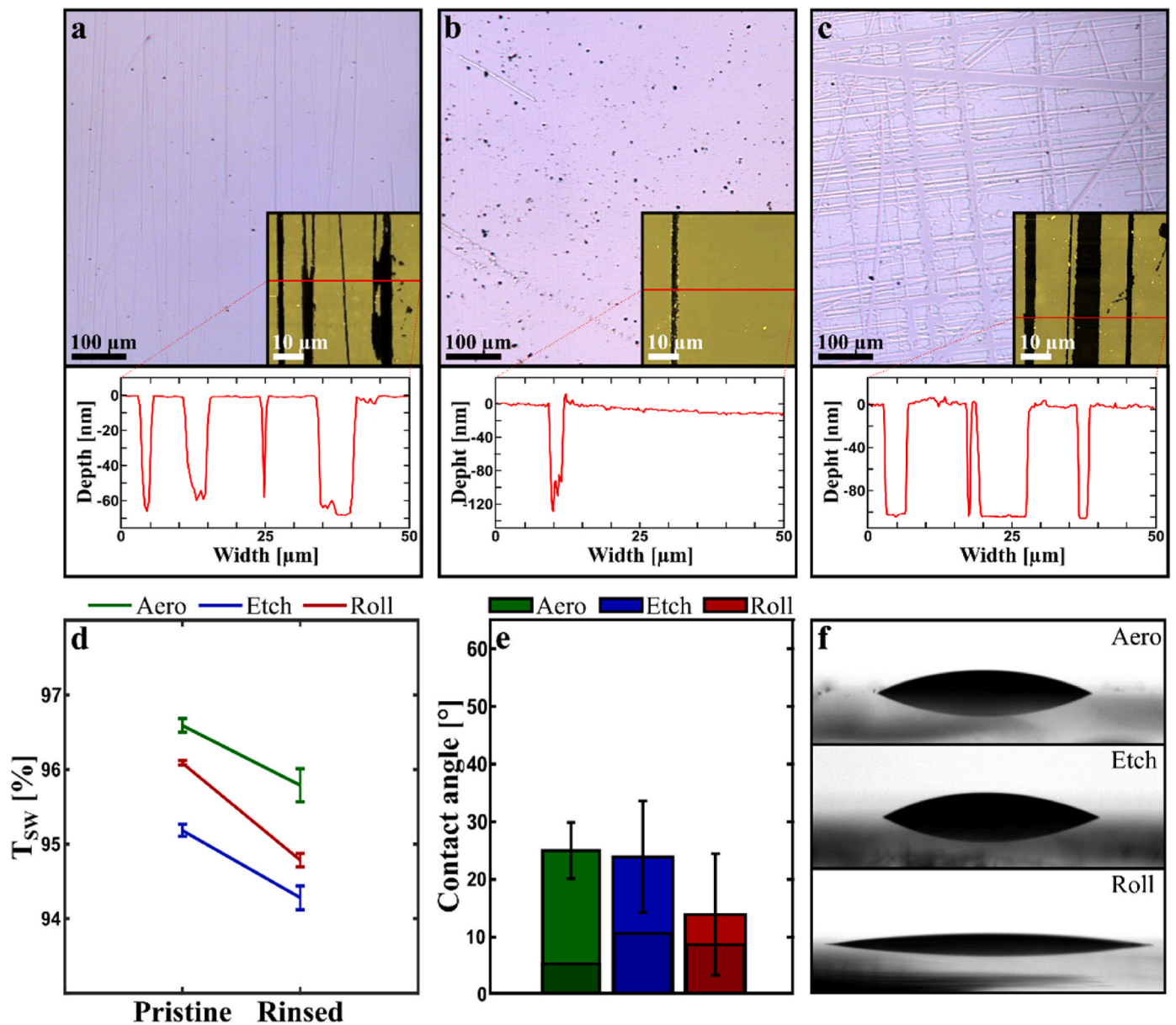
Fig. 7. Characterization after abrasion test. The optical microscope images show that AR_{Etch} is more prone to point defects than scratches (b), while both AR_{Aero} (a) and AR_{Roll} (c) exhibit numerous scratches, but more pronounced and deeper for AR_{Roll}. The coatings show similar reductions in average T_{SW} of approximately 1% (d). The water contact angle increased to ca. 25° for AR_{Aero} and AR_{Etch}, a bit more than the 14° of AR_{Roll} (e), but they are all still strongly hydrophilic (f).

deficiencies is damp heat, where the closed pore structure proved insufficient in resisting the chemical degradation caused by the prolonged exposure to humidity at elevated temperature.

Wettability is the property exhibiting the most stable behavior through all tests (even damp heat). The water contact angle of all coatings increases (as expected), largely attributed to soiling, but the surfaces remained hydrophilic, with the largest change observed after the humidity freeze test. Consequently, the self-cleaning properties and reduced risk of droplet scattering and fog formation, which makes hydrophilic AR coatings preferable over hydrophobic ones, are maintained [95].

The presented results suggest that the AR_{Aero} coating could be highly competitive, particularly in tempered and arid climates, where resistance to temperature variations, moderate humidity and sand erosion are central. The niche of desert climates could be especially interesting considering the challenge of utilizing the abundance of solar irradiance due to soiling and irreversible sand erosion as the dominant degrading

process [32,102]. Furthermore, primarily due to a better positioned transmittance peak than AR_{Etch}, and better durability than AR_{Roll}, and secondly due to the broadband antireflective behavior and closed porous surface (both originating from the hexagonal structure) [27], AR_{Aero} would be superior for applications in photovoltaics [11].

Now, as shown in our previous publication [27], increased T_{SW} gives a leveraged increase in thermal energy yield for a solar collector field due to the constant working temperature. Consequently, in an arid climate, the combined effect of 0.6% higher initial T_{SW} and a smaller reduction due to sand erosion (based on the abrasion test), an AR_{Aero} coated cover glass would improve the annual yield with up to 1.3% and 1.9% compared to AR_{Etch} and AR_{Roll}, respectively.

Finally, we note that the AR_{Aero} coating has been optimized with regards to optical properties and a closed pore structure [27]. Consequently, further optimization, for example calcination at a higher temperature, giving opportunity for simultaneous tempering, could potentially improve the mechanical properties and resistance to
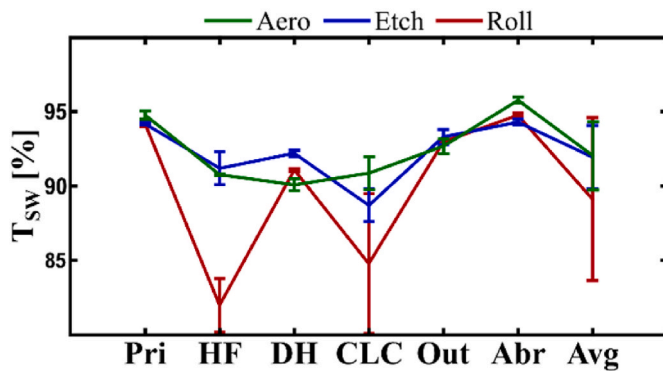
Fig. 8. Summary of optical properties. The solar weighted transmittance (T_{SW}) of low iron float glass with the different coatings is presented for pristine (Pri) samples, after the different durability tests (HF, DH, CLC, Out and Abr being humidity freeze, damp heat, industrial climate chamber test, outdoor exposure and abrasion resistance, respectively) and as an average of before and after tests (Avg). The AR_{Aero} coating exhibits comparable or even superior transmittance to the commercial coatings.

humidity of the AR_{Aero} coating, making it even more competitive [81].

5. Conclusions

An antireflective sol-gel silica coating with a closed hexagonal pore structure (AR_{Aero}) has been benchmarked against two commercial coatings with open pore structure, produced with acid etching (AR_{Etch}) and sol-gel roll coating (AR_{Roll}), respectively. The pristine coatings, though significantly different in terms of pore structures, exhibit similar mechanical properties and water contact angle, being superhydrophilic, but AR_{Aero} has a higher solar weighted transmittance.

The durability of the coatings was investigated thoroughly with regards to humidity, temperature, and abrasion resistance, by characterizing morphology, transmittance, wettability, and mechanical aspects following humidity freeze, damp heat, industrial climate chamber test, outdoor exposure, and abrasion and washability tests. Overall, AR_{Aero} performed on par or better than the commercial coatings, exhibiting a superior resistance to abrasion and dry soiling as well as humidity and temperature over moderate duration, benefits partially attributed to the closed pore structure. Only prolonged exposure to humidity at elevated temperatures proved detrimental to the AR_{Aero} coating due to chemical degradation. However, the coatings remained hydrophilic after all tests, and have consequently maintained the associated self-cleaning and optically beneficial properties.

The evident resistance to temperature variation, abrasion and moderate humidity makes the AR_{Aero} coating a competitive alternative well suited for tempered and arid climates. If used in such climates, the superior pristine transmittance and durability would manifest as a significantly higher yield from solar harvesting devices like solar collectors and photovoltaics.

Data availabilty

The data is available upon request to corresponding author.

CRediT authorship contribution statement

Erik Zäll: Writing – review & editing, Writing – original draft, Visualization, Validation, Methodology, Investigation, Formal analysis, Data curation, Conceptualization. **Stefan Karlsson:** Writing – review & editing, Writing – original draft, Visualization, Validation, Methodology, Investigation, Formal analysis, Data curation, Conceptualization. **Mikael Järn:** Writing – review & editing, Writing – original draft, Visualization, Validation, Methodology, Investigation, Formal analysis, Data curation, Conceptualization. **Jonas Segervald:** Writing – review & editing, Visualization, Methodology, Investigation, Formal analysis, Data curation. **Petter Lundberg:** Writing – review & editing, Investigation, Formal analysis, Data curation. **Thomas Wågberg:** Writing – review & editing, Validation, Supervision, Resources, Methodology, Investigation, Conceptualization.

Declaration of competing interest

The authors declare that they have no known competing financial interests or personal relationships that could have appeared to influence the work reported in this paper.

Data availability

Data will be made available on request.

Appendix A. Supplementary data

Supplementary data to this article can be found online at https://doi.org/10.1016/j.solmat.2023.112521.

References

[1] G.H. Brundtland, Our common future—call for action, Environ. Conserv. 14 (4) (1987) 291–294.

[2] D. Griggs, et al., Sustainable development goals for people and planet, Nature 495 (7441) (2013) 305–307, https://doi.org/10.1038/495305a.

[3] Unuited Nations, The Sustainable Development Goals Report 2022, 2022. Accessed: 2012-06-11. [Online]. Available: https://unstats.un.org/sdgs/report/2022/.

[4] United Nations, Glasgow climate pact - decision -/CP.26, Accessed: 2023-06-11. [Online]. Available: https://unfccc.int/documents/310497, 2021.

[5] E. Kabir, et al., Solar energy: potential and future prospects, Renew. Sustain. Energy Rev. 82 (2018) 894–900, https://doi.org/10.1016/j.rser.2017.09.094.

[6] W. Weiss, M. Spörk-Dür, Solar Heat Worldwide 2022, International Energy Agency, 2022. Accessed: 2023-06-11. [Online]. Available: https://www.iea-shc.org/solar-heat-worldwide.

[7] IEA, Renewables 2021 - analysis and forecast to 2026, in: International Energy Agency, 2021, 2026-06-11. [Online]. Available: https://www.iea.org/reports/renewables-2021.

[8] E. Zäll, et al., Environmentally sustainable electroplating of selective cobalt-chromium coating on stainless steel for efficient solar collectors, Sol. Energy Mater. Sol. Cell. 245 (2022), https://doi.org/10.1016/j.solmat.2022.111821.

[9] S. Kalogirou, The potential of solar industrial process heat applications, Appl. Energy 76 (4) (2003) 337–361, https://doi.org/10.1016/S0306-2619(02)00176-9.

[10] A. Fernández-García, et al., A parabolic-trough collector for cleaner industrial process heat, J. Clean. Prod. 89 (2015) 272–285, https://doi.org/10.1016/j.jclepro.2014.11.018.

[11] B.L. Allsopp, et al., Towards improved cover glasses for photovoltaic devices, Prog. Photovoltaics Res. Appl. 28 (11) (2020) 1187–1206, https://doi.org/10.1002/pip.3334.

[12] C. Ballif, J. Dicker, D. Borchert, T. Hofmann, Solar glass with industrial porous SiO2 antireflection coating: measurements of photovoltaic module properties improvement and modelling of yearly energy yield gain, Sol. Energy Mater. Sol. Cell. 82 (3) (2004) 331–344, https://doi.org/10.1016/j.solmat.2003.12.004.

[13] K.H. Nielsen, T. Kittel, K. Wondraczek, L. Wondraczek, Optical breathing of nanoporous antireflective coatings through adsorption and desorption of water, Sci. Rep. 4 (2014) 6595, https://doi.org/10.1038/srep06595.

[14] N. Sharma, et al., Design and deposition of single and multilayer antireflection coatings of glass substrate using electron beam deposition, Mater. Today: Proc. 5 (2) (2018) 6421–6425, https://doi.org/10.1016/j.matpr.2017.12.254.

[15] H. Nagel, A. Metz, R. Hezel, Porous SiO₂ films prepared by remote plasma-enhanced chemical vapour deposition – a novel antireflection coating technology for photovoltaic modules, Sol. Energy Mater. Sol. Cell. 65 (1) (2001) 71–77, https://doi.org/10.1016/S0927-0248(00)00079-9.

[16] K.H. Nielsen, et al., Large area, low cost anti-reflective coating for solar glasses, Sol. Energy Mater. Sol. Cell. 128 (2014) 283–288, https://doi.org/10.1016/j.solmat.2014.05.034.

[17] H. Dislich, Sol-gel: science, processes and products, J. Non-Cryst. Solids 80 (1) (1986) 115–121, https://doi.org/10.1016/0022-3093(86)90384-4.

[18] D. Chen, Anti-reflection (AR) coatings made by sol-gel processes: a review, Sol. Energy Mater. Sol. Cell. 68 (2001) 313–336, https://doi.org/10.1016/S0927-0248(00)00365-2.

[19] D. Adak, R. Bhattacharyya, H.C. Barshilia, A state-of-the-art review on the multifunctional self-cleaning nanostructured coatings for PV panels, CSP mirrors and related solar devices, Renew. Sustain. Energy Rev. 159 (2022), https://doi.org/10.1016/j.rser.2022.112145.

[20] Z.Q. Guo, et al., Super-durable closed-surface antireflection thin film by silica nanocomposites, Sol. Energy Mater. Sol. Cell. 170 (2017) 143–148, https://doi.org/10.1016/j.solmat.2017.05.043.

[21] J. Chen, et al., A facile strategy to prepare antireflection coatings with high transmittance and improved mechanical stability and application in crystalline silicon solar modules, J. Sol. Gel Sci. Technol. 103 (2) (2022) 360–366, https://doi.org/10.1007/s10971-022-05790-4.

[22] X. Wang, et al., Durable superhydrophilic and antireflective coating for high-performance anti-dust photovoltaic systems, Appl. Nanosci. 11 (3) (2021) 875–885, https://doi.org/10.1007/s13204-020-01643-0.

[23] X. Li, et al., Fabrication of single-layer antireflective coating with environmental stability by modified SiO₂ mixed sol, Colloids Surf. A Physicochem. Eng. Asp. 630 (2021), https://doi.org/10.1016/j.colsurfa.2021.127553.

[24] C. Agustín-Sáenz, M. Machado, A. Tercjak, Polyfluoroalkyl-silica porous coatings with high antireflection properties and low surface free energy for glass in solar energy application, Appl. Surf. Sci. 509 (2020), https://doi.org/10.1016/j.apsusc.2019.144864.

[25] M. Zettl, High performance coatings for solar receivers and new dedicated manufacturing solution, Energy Proc. 48 (2014) 701–706, https://doi.org/10.1016/j.egypro.2014.02.081.

[26] G. San Vicente, R. Bayón, N. Germán, A. Morales, Long-term durability of sol–gel porous coatings for solar glass covers, Thin Solid Films 517 (10) (2009) 3157–3160, https://doi.org/10.1016/j.tsf.2008.11.079.

[27] E. Zäll, et al., Aerosol-based deposition of broadband antireflective silica coating with closed mesoporous structure, Sol. Energy Mater. Sol. Cell. 250 (2023), https://doi.org/10.1016/j.solmat.2022.112078.

[28] B. Perers, et al., Long term testing and evaluation of PV modules with and without sunarc antireflective coating of the cover glass, Energy Proc. 70 (2015) 311–317, https://doi.org/10.1016/j.egypro.2015.02.128.

[29] Y. Ota, M. Ahmad, K. Nishioka, A 3.2% output increase in an existing photovoltaic system using an anti-reflection and anti-soiling silica-based coat, Sol. Energy 136 (2016) 547–552, https://doi.org/10.1016/j.solener.2016.07.038.

[30] I. Arabatzis, et al., Photocatalytic, self-cleaning, antireflective coating for photovoltaic panels: characterization and monitoring in real conditions, Sol. Energy 159 (2018) 251–259, https://doi.org/10.1016/j.solener.2017.10.088.

[31] W. Kong, et al., Side by side tests of two SDHW systems with solar collectors with and without antireflection treatment, Energy Proc. 70 (2015) 462–469, https://doi.org/10.1016/j.egypro.2015.02.148.

[32] R. Conceição, J. González-Aguilar, A.A. Merrouni, M. Romero, Soiling effect in solar energy conversion systems: a review, Renew. Sustain. Energy Rev. 162 (2022), https://doi.org/10.1016/j.rser.2022.112434.

[33] G. Womack, et al., The performance and durability of single-layer sol-gel anti-reflection coatings applied to solar module cover glass, Surf. Coating. Technol. 358 (2019) 76–83, https://doi.org/10.1016/j.surfcoat.2018.11.030.

[34] A.S. Sarkın, N. Ekren, Ş. Sağlam, A review of anti-reflection and self-cleaning coatings on photovoltaic panels, Sol. Energy 199 (2020) 63–73, https://doi.org/10.1016/j.solener.2020.01.084.

[35] L. Wang, M. Liu, Y. Wu, H. Zheng, Progress in studies of surface nanotextures and coatings with nanomaterials on glass for anti-dust functionality, Nanomaterials 12 (20) (2022), https://doi.org/10.3390/nano12203677.

[36] M. Abraim, et al., Techno-economic assessment of soiling losses in CSP and PV solar power plants: a case study for the semi-arid climate of Morocco, Energy Convers. Manag. 270 (2022), https://doi.org/10.1016/j.enconman.2022.116285.

[37] P. Bellmann, F. Wolfertstetter, R. Conceição, H.G. Silva, Comparative modeling of optical soiling losses for CSP and PV energy systems, Sol. Energy 197 (2020) 229–237, https://doi.org/10.1016/j.solener.2019.12.045.

[38] S.C. Pop, et al., A highly abrasive-resistant, long-lasting anti-reflective coating for PV module glass, IEEE 40th Photovoltaic Specialist Conference (2014) (2014) 2715–2719, https://doi.org/10.1109/PVSC.2014.6925490. PVSC).

[39] C.-H. Chen, et al., Scratch-resistant zeolite anti-reflective coating on glass for solar applications, Sol. Energy Mater. Sol. Cell. 95 (7) (2011) 1694–1700, https://doi.org/10.1016/j.solmat.2011.01.032.

[40] M.C. Bautista, A. Morales, Silica antireflective films on glass produced by the sol–gel method, Sol. Energy Mater. Sol. Cell. 80 (2) (2003) 217–225, https://doi.org/10.1016/j.solmat.2003.06.004.

[41] H. Ye, et al., Preparation of antireflective coatings with high transmittance and enhanced abrasion-resistance by a base/acid two-step catalyzed sol–gel process, Sol. Energy Mater. Sol. Cell. 95 (8) (2011) 2347–2351, https://doi.org/10.1016/j.solmat.2011.04.004.

[42] K.H. Nielsen, S. Karlsson, R. Limbach, L. Wondraczek, Quantitative image analysis for evaluating the abrasion resistance of nanoporous silica films on glass, Sci. Rep. 5 (2015), 17708, https://doi.org/10.1038/srep17708.

[43] G. Helsch, M. Krzyzak, G. Heide, G.H. Frischat, Adherent antireflection coatings on borosilicate glass for solar collectors, Glass Technol. Eur. J. Glass Sci. Technol. 47 (5) (2006) 153–156.

[44] K. Cathro, D. Constable, T. Solaga, Silica low-reflection coatings for collector covers, by a dip-coating process, Sol. Energy 32 (5) (1984) 573–579, https://doi.org/10.1016/0038-092X(84)90131-2.

[45] P. Belleville, H. Floch, Ammonia Hardening of Porous Silica Antireflective Coatings, SPIE's 1994 International Symposium On Optics, Imaging, and Instrumentation, 1994, https://doi.org/10.1117/12.188957.

[46] C. Cai, et al., Robust anti-reflective silica nanocoatings: abrasion resistance enhanced via capillary condensation of APTES, J. Mater. Chem. C 3 (17) (2015) 4254–4259, https://doi.org/10.1039/C5TC00357A.

[47] F. Chi, et al., Enhancing mechanical stability of sol–gel silica antireflection coatings via ammonia treatment at low temperature, Results Phys. 18 (2020), https://doi.org/10.1016/j.rinp.2020.103315.

[48] C. Tao, L. Zhang, Fabrication of multifunctional closed-surface SiO₂-TiO₂ antireflective thin films, Colloids Surf. A Physicochem. Eng. Asp. 585 (2020), https://doi.org/10.1016/j.colsurfa.2019.124045.

[49] Z. Guo, et al., Closed-surface multifunctional antireflective coating made from SiO₂ with TiO₂ nanocomposites, Materials 14 (6) (2021), https://doi.org/10.3390/ma14061367.

[50] J. Li, et al., Design, preparation, and durability of TiO₂/SiO₂ and ZrO₂/SiO₂ double-layer antireflective coatings in crystalline silicon solar modules, Sol. Energy 89 (2013) 134–142, https://doi.org/10.1016/j.solener.2012.12.011.

[51] G. Helsch, J. Deubener, Compatibility of antireflective coatings on glass for solar applications with photocatalytic properties, Sol. Energy 86 (3) (2012) 831–836, https://doi.org/10.1016/j.solener.2011.12.010.

[52] H. Trung Tran, et al., Characterization of closed-surface antireflective TiO₂–SiO₂ films for application in solar-panel glass, Mater. Lett. 326 (2022), https://doi.org/10.1016/j.matlet.2022.132921.

[53] M.S. Mozumder, A.-H.I. Mourad, H. Pervez, R. Surkatti, Recent developments in multifunctional coatings for solar panel applications: a review, Sol. Energy Mater. Sol. Cell. 189 (2019) 75–102, https://doi.org/10.1016/j.solmat.2018.09.015.

[54] Z.-S. Huang, et al., Experimental investigation of the anti-soiling performances of different wettability of transparent coatings: superhydrophilic, hydrophilic, hydrophobic and superhydrophobic coatings, Sol. Energy Mater. Sol. Cell. 225 (2021), https://doi.org/10.1016/j.solmat.2021.111053.

[55] J. Wang, et al., Highly stable and efficient mesoporous and hollow silica antireflection coatings for perovskite solar Cells, ACS Appl. Energy Mater. 3 (5) (2020) 4484–4491, https://doi.org/10.1021/acsaem.0c00175.

[56] T. Salamah, et al., Effect of dust and methods of cleaning on the performance of solar PV module for different climate regions: comprehensive review, Sci. Total Environ. 827 (2022), 154050, https://doi.org/10.1016/j.scitotenv.2022.154050.

[57] U. Mehmood, et al., Superhydrophobic surfaces with antireflection properties for solar applications: a critical review, Sol. Energy Mater. Sol. Cell. 157 (2016) 604–623, https://doi.org/10.1016/j.solmat.2016.07.038.

[58] J. Chen, et al., Facile fabrication of antifogging, antireflective, and self-cleaning transparent silica thin coatings, Colloids Surf. A Physicochem. Eng. Asp. (2016), https://doi.org/10.1016/j.colsurfa.2016.08.037.

[59] A. Eshaghi, M. Mojab, Fabrication of antireflective antifogging nano-porous silica thin film on glass substrate by layer-by-layer assembly method, J. Non-Cryst. Solids 405 (2014) 148–152, https://doi.org/10.1016/j.jnoncrysol.2014.09.017.

[60] X. Du, et al., Broadband antireflective superhydrophilic antifogging nano-coatings based on three-layer system, Microporous Mesoporous Mater. 255 (2018) 84–93, https://doi.org/10.1016/j.micromeso.2017.07.017.

[61] X. Sun, et al., Preparation of hydrophobic SiO₂/PTFE sol and antireflective coatings for solar glass cover, Optik 212 (2020), https://doi.org/10.1016/j.ijleo.2020.164704.

[62] H. Salehi, A. Eshaghi, M. Rezazadeh, H. Zabolian, Antireflective and anti-dust modified silica based thin film on solar cell cover glass, J. Alloys Compd. 892 (2022), https://doi.org/10.1016/j.jallcom.2021.162228.

[63] X. Wang, et al., Surface free energy and microstructure dependent environmental stability of sol–gel SiO₂ antireflective coatings: effect of combined vapor phase surface treatment, J. Colloid Interface Sci. 555 (2019) 124–131, https://doi.org/10.1016/j.jcis.2019.07.056.

[64] J. Xu, et al., Superhydrophobic silica antireflective coatings with high transmittance via one-step sol-gel process, Thin Solid Films 631 (2017) 193–199, https://doi.org/10.1016/j.tsf.2017.03.005.

[65] A. Gruzd, et al., All-nanoparticle monolayer broadband antireflective and self-cleaning transparent glass coatings, ACS Appl. Mater. Interfaces 13 (5) (2021) 6767–6777, https://doi.org/10.1021/acsami.0c18776.

[66] M. Poddighe, P. Innocenzi, Hydrophobic thin films from sol-gel processing: a critical review, Materials 14 (22) (2021), https://doi.org/10.3390/ma14226799.

[67] C. Agustín-Sáenz, M. Machado, O. Zubillaga, A. Tercjak, Hydrophobic and spectrally broadband antireflective methyl-silylated silica coatings with high

performance stability for concentrated solar applications, Sol. Energy Mater. Sol. Cell. 200 (2019), https://doi.org/10.1016/j.solmat.2019.109962.

[68] A. Pouladian-Kari, et al., A novel solution for addressing the problem of soiling and improving performance of PV solar systems, Sol. Energy 241 (2022) 315–326, https://doi.org/10.1016/j.solener.2022.06.012.

[69] D. Dahlioui, L. Traore, B. Laarabi, A. Barhdadi, Ecological cleaning of PV panels by exploitation of dew water in Morocco, Mater. Today: Proc. 66 (2022) 130–134, https://doi.org/10.1016/j.matpr.2022.04.024.

[70] J. Harra, et al., Characteristics of nFOG, an aerosol-based wet thin film coating technique, J. Coating Technol. Res. 15 (3) (2018) 623–632, https://doi.org/10.1007/s11998-017-0022-7.

[71] M. Touminen, M. Järn, S. Tammela, Mesoporous SiO2-Coatings on Glass by a Novel Aerosol Based Coating Method Called nFOG, Presented at *the Aerosol Technology*, Tampere, Finland, 2015.

[72] A. Syafiq, A.K. Pandey, N.N. Adzman, N.A. Rahim, Advances in approaches and methods for self-cleaning of solar photovoltaic panels, Sol. Energy 162 (2018) 597–619, https://doi.org/10.1016/j.solener.2017.12.023.

[73] A.S.H. Makhlouf, Current and advanced coating technologies for industrial applications, in: Nanocoatings and Ultra-thin Films, Woodhead Publishing Limited, 2011, pp. 3–23.

[74] IEC Standard 62108:2016, Concentrator Photovoltaic (CPV) Modules and Assemblies – Design Qualification and Type Approval, International Electrotechnical Commission, 2016.

[75] H.E. Beck, et al., Present and future Koppen-Geiger climate classification maps at 1-km resolution, Sci. Data 5 (2018), 180214, https://doi.org/10.1038/sdata.2018.214.

[76] ASTM Standard D3450, Standard test method for washability properties of interior architectural coatings, ASTM International, 2015.

[77] EN Standard 410:2011 - Glass in Building - Determination of Luminous and Solar Characteristics of Glazing, European Standards, 2011.

[78] ASTM Standard G173, Standard Tables for Reference Solar Spectral Irradiances: Direct Normal and Hemispherical on 39° Tilted Surface, ASTM International, 2020.

[79] ISO Standard 15472:2010, Surface Chemical Analysis - X-Ray Photoelectron Spectrometers - Calibration of Energy Scales, International Organization for Standardization, 2010.

[80] W.C. Oliver, G.M. Pharr, An improved technique for determining hardness and elastic modulus using load and displacement sensing indentation experiments, J. Mater. Res. 7 (1992) 1564–1583, https://doi.org/10.1557/JMR.1992.1564.

[81] P. Sundberg, et al., Simultaneous chemical vapor deposition and thermal strengthening of glass, Thin Solid Films 669 (2019) 487–493, https://doi.org/10.1016/j.tsf.2018.11.028.

[82] Y. Kato, H. Yamazaki, S. Yoshida, J. Matsuoka, Effect of densification on crack initiation under Vickers indentation test, J. Non-Cryst. Solids 356 (35–36) (2010) 1768–1773, https://doi.org/10.1016/j.jnoncrysol.2010.07.015.

[83] M. Wada, H. Furukawa, K. Fujita, Crack resistance of glass on Vickers indentation, in X international congress on glass (ICG), Kyoto, Japan 11 (1974) 39–46.

[84] H. Yan, et al., Nanoscale etching of microporous coatings for broadband antireflection coatings, Thin Solid Films 698 (2020), https://doi.org/10.1016/j.tsf.2020.137858.

[85] N.J. Hutchinson, et al., Reflectance of surfactant-templated mesoporous silica thin films: simulations versus experiments, Thin Solid Films 518 (8) (2010) 2134–2140, https://doi.org/10.1016/j.tsf.2009.08.006.

[86] M. Rubin, Optical properties of soda lime silica glasses, Sol. Energy Mater. 12 (4) (1985) 275–288, https://doi.org/10.1016/0165-1633(85)90052-8.

[87] R.S.A. Kanta, J. Ralston, Thermally- and photoinduced changes in the water wettability of low-surface-area Silica and Titania, Langmuir 21 (2005) 2400–2407, https://doi.org/10.1021/la047721m.

[88] S. Takeda, Surface OH group governing wettability of commercial glasses, J. Non-Cryst. Solids 249 (1999) 41–46, https://doi.org/10.1016/S0022-3093(99)00297-5.

[89] T. Suzuki, T. Sekine, K. Yamamoto, K. Fukutani, Change in the surface OH group on soda lime silicate glass and silica glass after heat treatment in nitrogen atmosphere, J. Non-Cryst. Solids 464 (2017) 89–91, https://doi.org/10.1016/j.jnoncrysol.2017.03.014.

[90] T.T. Chau, W.J. Bruckard, P.T. Koh, A.V. Nguyen, A review of factors that affect contact angle and implications for flotation practice, Adv. Colloid Interface Sci. 150 (2) (2009) 106–115, https://doi.org/10.1016/j.cis.2009.07.003.

[91] J. Bico, U. Thiele, D. Que're', Wetting of textured surfaces, Colloids Surf. A Physicochem. Eng. Asp. 206 (2002) 41–46, https://doi.org/10.1016/S0927-7757(02)00061-4.

[92] A. Marmur, Contact angle in constrained wetting, Langmuir 12 (1996) 5704–5708, https://doi.org/10.1021/la950828c.

[93] S. Takeda, M. Fukawa, Y. Hayashi, K. Matsumoto, Surface OH group govern adsorption properties of metal oxide films, Thin Solid Films 339 (1999) 220–224, https://doi.org/10.1016/S0040-6090(98)01152-3.

[94] Y.A. Gösterişlioğlu, A.E. Ersundu, M. Çelikbilek Ersundu, İ. Sökmen, Investigation the effect of weathering on chemically strengthened flat glasses, J. Non-Cryst. Solids 544 (2020), 120192, https://doi.org/10.1016/j.jnoncrysol.2020.120192.

[95] A. Syafiq, et al., Application of transparent self-cleaning coating for photovoltaic panel: a review, Curr. Opin. Chem. Eng. 36 (2022), https://doi.org/10.1016/j.coche.2022.100801.

[96] K.R. McIntosh, X. Dai, Damp-heat degradation and repair of oxide-passivated silicon, Phys. Status Solidi 208 (8) (2011) 1931–1936, https://doi.org/10.1002/pssa.201026492.

[97] V. Guiheneuf, et al., Investigation of damp heat effects on glass properties for photovoltaic applications, Corrosion Eng. Sci. Technol. 52 (3) (2016) 170–177, https://doi.org/10.1080/1478422x.2016.1234803.

[98] E. Choi, S. Kim, Surface pH buffering to promote degradation of mesoporous silica nanoparticles under a physiological condition, J. Colloid Interface Sci. 533 (2019) 463–470, https://doi.org/10.1016/j.jcis.2018.08.088.

[99] J.A.G. Rodriguez, R.J. Hand, Evolution of the modulus and hardness of the tin and air sides of float glass as a function of hydration time, Glass Technol. Eur. J. Glass Sci. Technol. 54 (1) (2013) 36–41.

[100] K. Hirao, M. Tomozawa, Kinetics of crack tip blunting of glasses, J. Am. Cera. Soc. 70 (1) (1987) 43–48, https://doi.org/10.1111/j.1151-2916.1987.tb04851.x.

[101] M. Sakhuja, et al., Outdoor performance and durability testing of antireflecting and self-cleaning glass for photovoltaic applications, Sol. Energy 110 (2014) 231–238, https://doi.org/10.1016/j.solener.2014.07.003.

[102] B. Agea-Blanco, C. Meyer, R. Müller, J. Günster, Sand erosion of solar glass: specific energy uptake, total transmittance, and module efficiency, Int. J. Energy Res. 42 (3) (2018) 1298–1307, https://doi.org/10.1002/er.3930.

[103] C. Xin, C. Peng, Y. Xu, J. Wu, A novel route to prepare weather resistant, durable antireflective films for solar glass, Sol. Energy 93 (2013) 121–126, https://doi.org/10.1016/j.solener.2013.04.006.

[104] C. Agustín-Sáenz, et al., Mechanical properties and field performance of hydrophobic antireflective sol-gel coatings on the cover glass of photovoltaic modules, Sol. Energy Mater. Sol. Cell. 216 (2020), https://doi.org/10.1016/j.solmat.2020.110694.